Nano Research
2023, 16(8): 11503–11510
ISSN 1998-0124 CN 11-5974/O4
https://doi.org/10.1007/s12274-023-5932-3

# Crystallization-assisted asymmetric assembly of polymer nanocrescents and fidelity carbon analogues: Experiment and simulation study

Lu Hou[1,§], Junfeng Wang[2,3,§], Sijia Wang[1], Wen-Cui Li[1], Guohui Li[2] (✉), and An-Hui Lu[1] (✉)

[1] *State Key Laboratory of Fine Chemicals, Liaoning Key Laboratory for Catalytic Conversion of Carbon Resources, School of Chemical Engineering, Dalian University of Technology, Dalian 116024, China*
[2] *Laboratory of Molecular Modeling and Design, State Key Laboratory of Molecular Reaction Dynamics, Dalian Institute of Chemical Physics, Chinese Academy of Sciences, Dalian 116023, China*
[3] *School of physics, Liaoning University, Shenyang 110036, China*
[§] *Lu Hou and Junfeng Wang contributed equally to this work.*

**Received:** 21 April 2023 / **Revised:** 10 June 2023 / **Accepted:** 14 June 2023

## ABSTRACT

Anisotropic nanoparticles, giving rise to a large number of novel physicochemical properties and functionalities, have provoked increasing attentions in nanoscience and nanotechnology. The remained challenge is to develop synthetic methods for the fabrication of anisotropic nanoparticles with less symmetry under the principle of minimum surface free energy. Here, we established a crystallization-assisted asymmetric assembly method for the synthesis of anisotropic polymer nanocrescents and their carbonaceous analogues by using triblock copolymer F127 and octadecanol in aqueous solution. With the aid of molecular dynamics (MD) simulation, we demonstrate that the observed crescent structure is caused by asymmetry distribution of octadecanol crystal within the hydrophobic core of F127 micelles, via the formation of intermediate elliptic micelles bearing hydrophobic ends that further fuse with each other end-to-end at an angle into curing nanocrescent morphology. The influences of annealing time, annealing temperature, and mole ratios of precursors that govern the kinetics of the assembly and polymerization process were systematically investigated and a series of polymer nanocrescents with tunable length of ~ 85 to ~ 262 nm and aspect ratio of ~ 1.1 to ~ 3.0 were prepared. The ability to create novel crescent-shaped polymer and carbon nanoparticles and the identification of asymmetric assembly process by combining experiment and simulation study will provide a valuable contribution both to theoretical and technological researches.

## KEYWORDS

polymer nanocrescent, carbon nanocrescent, asymmetric assembly, micelle, crystallization, molecular simulation

## 1 Introduction

The assembled synthesis of carbon nanomaterials with well-defined structures has been a long challenge task because they can be harnessed to help solve the issues in many application fields such as energy storage [1, 2], biological medicine [3, 4], catalysis [5, 6], and adsorption [7, 8]. In particular, much current research has been driven by anisotropic carbon materials characterized by discrepant morphology features or physicochemical properties in various directions [9]. The advances in the preparation of anisotropic materials have provided a new dimension to nanoscience due to their unusual optical [10, 11], electrical [12, 13], and photothermal [14, 15] properties compared with their higher symmetric counterparts. However, limited success has been achieved by liquid phase assembled synthesis. Dominated by the minimization of interface free energy, nanoparticles are usually formed in spherical shape with isotropic properties. The ability to synthesize new forms of anisotropic nanoparticles will open up a mass of new possibilities for their applications in electronic devices [16], drug delivery [17, 18], colloidal superstructures [19], and even theoretical research [20].

As a specific kind of anisotropic particle, crescent-shaped nanoparticle, with two directional sharp edges, has become a candidate in the fields of surface-enhanced fluorescence, surface-enhanced Raman spectroscopy, and plasmon resonance energy transfer [21–23]. Generally, the nanocrescents are fabricated by "top-down" approaches like e-beam lithography and nanosphere lithography [24, 25], and their elements are confined to noble metals mostly [26]. There is an urgent demand for novel preparation methods saving both time and labor. Till now, there only exists limited success which conducted free-standing nanocrescents utilizing laboratory-made peptide-based building blocks [27]. These systems are based on biomacromolecules, which are not applicable to preparing thermally stable polymer and even carbon fidelity analogues. Despite numerous advances in the development of novel carbon materials, the detailed synthesis of carbon nanocrescents has not been proposed yet. Therefore, it's necessary to propose an effective synthetic strategy for the carbon nanocrescents. Meanwhile, the kinetics mechanism of morphology transition is discussed in detail, which will encourage

---

Address correspondence to Guohui Li, ghli@dicp.ac.cn; An-Hui Lu, anhuilu@dlut.edu.cn

researchers to figure out how to build anisotropic nanoparticles by liquid phase synthesis chemistry.

In our previous work, the synthetic strategy of an asymmetric intramicellar phase-transition induced tip-to-tip assembly has been developed for the preparation of polymer and carbon nanorings, and a morphology transition process from nanocrescents to nanorings is observed [28]. As an indispensable intermediate, nanocrescents are crucial to the ring-forming process. However, the underlying formation mechanism and an effective synthetic strategy for size-controlled nanocrescents have not been discovered and developed. Hence, in the present study, we established a crystallization-assisted asymmetric assembled synthesis of polymer nanocrescents and their carbonaceous fidelity analogues based on the structure-directing role of crescent micelles assembled from triblock copolymer F127 and crystalline octadecanol. Nanocrescents with tunable length and aspect ratio can be readily regulated by altering the synthetic conditions. Molecular dynamics (MD) simulations were carried out for the fundamental understanding of the formation mechanism of the crescent micelles, as well as the morphology transformation with respect to annealing temperature and octadeconal/F127 mole ratio. We show that elliptic micelles, with ends bearing partially exposed hydrophobic core, were firstly formed by the asymmetric distribution of octadecanol crystal in F127 coronal. Then, the obtained elliptic micelles fused with each other end-to-end at an angle, leading to the formation of crescent micelles.

## 2 Experimental section

### 2.1 Materials

Resorcinol (99.5%), ammonia solution (25 wt.%), propylamine (98.5 wt.%), formaldehyde (37 wt.%), and octadecanol were obtained from Sinopharm Chemical Reagent Co., Ltd. Pluronic F127 was purchased from Sigma. All chemicals were used without further purification.

### 2.2 Synthesis of crescent-shaped micelles

In a typical procedure, F127 (800 mg) was first dissolved in deionized water (80 mL), then octadecanol (85.7 mg) was added. The hot solution was stirred vigorously to form a uniform microemulsion, followed by a quick transfer to a water bath of 28 °C for 0.5 h. Then, a microemulsion of crescent-shaped F127/octadecanol micelles with a shallow milky appearance was achieved.

### 2.3 Synthesis of polymer nanocrescents

Resorcinol (110 mg) and formaldehyde (38%) (146 μL) were dissolved in water (90 mL) at 20 °C for half an hour. Then, microemulsion of F127/octadecanol micelle (10 mL) was added to the solution mixture. After that, propylamine solution (0.25 mL, 1 M) and ammonia solution (0.25 mL, 1.5 M) were added in sequence with gentle stirring for 1 h. The white dispersion was further heated to 70 °C for 4 h. Finally, the polymer nanocrescents were collected by centrifugation, rinsing three times, and freeze-drying.

### 2.4 Synthesis of carbon nanocrescents

The as-prepared polymer nanocrescents were calcination at 600 °C for 2 h under an argon atmosphere to achieve carbon nanocrescents.

### 2.5 MD simulations

The LAMMPS program was used for carrying out MD simulations of the self-assembly of F127 and octadecanol molecules [29]. All simulation systems were carried out in the canonical (NVT) ensemble at 8 or 48 °C with implicit solvents. The velocity-Verlet algorithm with a time step of 0.05 ps and the Langevin equation were used for integrating the equations of motion and temperature. The cut-off LJ potentials were used to describe the interaction between every two particles, and the interaction parameters referred to the Dry Martini force field [30]. All the systems were carried out on a 100 nm × 100 nm × 100 nm, and the morphologies were observed by OVITO [31]. To solve the barrier of spatial scale between the simulation system and the experimental system, the self-assembly process was simulated by the step-by-step method. The detailed simulation process is introduced in Section S1 in the Electronic Supplementary Material (ESM).

### 2.6 Characterization

The detailed characterization information is given in Section S2 in the ESM.

## 3 Result and discussion

### 3.1 Asymmetric assembled synthesis of polymer and carbon nanocrescents

The polymer and carbon nanocrescents were synthesized based on the asymmetric assembly of F127 and octadecanol, and the synthetic route is presented in Fig. 1(a). Bi-component micelles with F127 coronal and molten octadecanol core were first formed through hydrophilic and hydrophobic interaction as the water is a poor solvent of hydrophobic octadecanol. After annealing the micelles below the melting point of octadecanol for crystallization and assembly, crescent micelles with two opposite tips were formed. The micelles were used as the soft templates, guiding the nucleation and growth of polymer precursors (resorcinol, formaldehyde, and n-propylamine) through abundant hydrogen bond interaction, and the faithful replicas of polymer nanocrescents were achieved. Finally, carbonaceous nanocrescents were obtained through fidelity morphology transformation after carbonization of polymer nanocrescents under an argon atmosphere.

The X-ray diffraction (XRD) pattern of crescent micelles is presented in Fig. 1(b), where the reflections of octadecanol crystal are clearly exhibited. The peaks located at around 21.8° and 24.6° can be assigned to monoclinic γ phase of octadecanol [32]. Scanning electron microscopy (SEM) image of the polymer nanocrescents in Fig. 1(c) revealed a crescent-shaped nanostructure with length along the long axis of ~ 116 nm and thickness along the short axis of ~ 77 nm. After carbonization at 600 °C, carbon nanocrescents were formed, as seen in Fig. 1(d). Noteworthy, the crescent-shaped morphology was faithfully retained, while the length and the thickness shrunk to ~ 87 and ~ 49 nm, respectively.

To explore the forming process of the crescent micelles, the morphology transformation of the micelles with annealing time was investigated. Since the micelles are vulnerable under SEM measurements, the morphologies of all samples were frozen by the polymerization process, making it easier for us to observe. As seen in Figs. 2(a)–2(c), the crescent micelles assembled quickly in 0.5 h and the morphology can be well-preserved with annealing time extending to 24 h. According to the statistics of 100 particles, we found that the length of nanocrescents increased from 116 to 184 and 189 nm, while the thickness increased from 77 to 107 and 117 nm with the annealing time prolonging from 0.5 to 12 and 24 h (Fig. 2(d)), due to the continuous assembly process. Noteworthy, the aspect ratio was relatively maintained at about

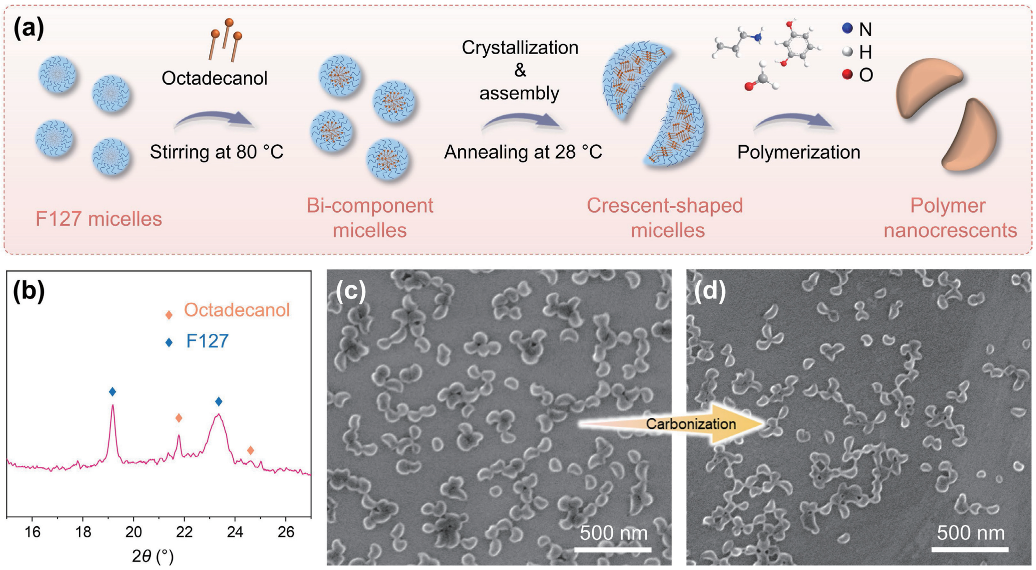

Figure 1 (a) Fabrication scheme of polymer and carbon nanocrescents. (b) The XRD pattern of crescent micelles. SEM images of (c) polymer and (d) carbon nanocrescents.

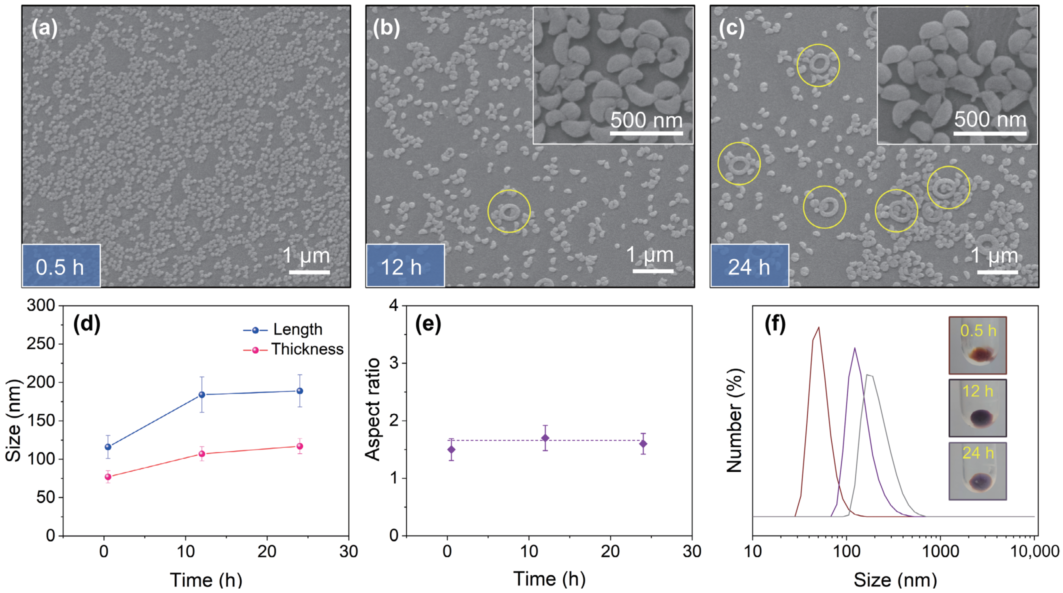

Figure 2 SEM images of polymer nanocrescents prepared based on different templates with annealing time of (a) 0.5, (b) 12, and (c) 24 h, respectively. The evolution of (d) length and thickness and (e) aspect ratio of the polymer nanocrescents along with the annealing time. (f) Dynamic light scattering (DLS) plots of micelles with different annealing time. Insets are optical photographs of polymer nanocrescents after high-speed centrifugation.

1.6, indicating the aspect ratio of the nanocrescents is not sensitive to the annealing time (Fig. 2(e)). The coexistence of nanocrescents and nanorings (Fig. 2(b), marked with yellow circles) was visible after 12 h annealing, which indicated that the crescent micelles spontaneously fuse with each other to form ringy superstructures along with the annealing process. And more ringy nanoparticles were formed after annealing for 24 h (Fig. 2(c), marked with yellow circles). The growth trend was firmly proved by the distributions of the hydrodynamic diameter of F127/octadecanol micelles dispersion at different annealing time (Fig. 2(f)). The average size, as well as the particle dispersion index (PDI), showed an upward trend due to the increase of nanocrescents size and the undesired ringy nanostructures. The morphology transition was also reflected in the color changes from dark red to grey of the centrifugal polymer products (the inset of Fig. 2(f)).

### 3.2 Temperature and mole ratio effects on nanocrescent size and aspect ratio

As known, the temperature is an essential parameter for crystallization and assembly process of micelle. Therefore, to understand the influence of annealing temperature on the morphology of nanocrescents, the micelle dispersions were cooled to a series of crystallization temperatures (8, 28, 38, and 48 °C) below the melting temperature ($T_m$) of octadecanol and annealed for 0.5 h before polymerization. After the exposure to a relatively low temperature (8 and 28 °C), monodispersed polymer nanocrescents with similar lengths (110 and 116 nm) and aspect ratios (1.36 and 1.5) were obtained, indicating a parallel assembly behavior (Figs. 2(a) and 3(a)). As the annealing temperature increased to 38 °C, an obvious stretch along the long axis of nanocrescents was detected (Fig. 3(b)), and thinner crescents with an aspect ratio of ~ 1.9 were obtained. With a further rise in annealing temperature, slender and curving nanostructures were formed, whose aspect ratio further increased to ~ 3.0 (Fig. 3(c)). The evolutions of the length and aspect ratio along with the annealing temperature are shown in Fig. 3(d). The results indicate that a higher annealing temperature would facilitate the loose packing of monomers and induce the assembly of F127/octadecanol micelles into slender nanocrescents, whereas the

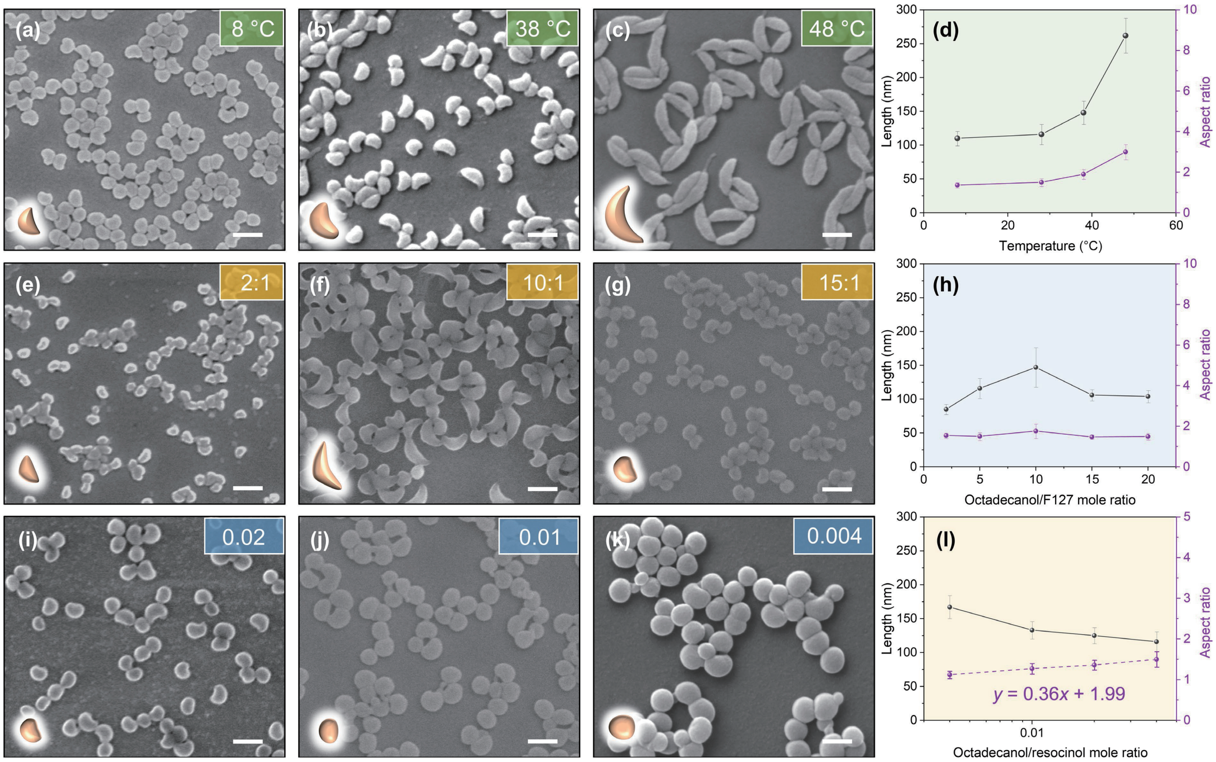

**Figure 3** SEM images of polymer nanocrescents prepared with different annealing temperatures of (a) 8, (b) 38, and (c) 48 °C, respectively. (d) The evolution of length and aspect ratio along with the annealing temperature. SEM images of polymer nanocrescents prepared with different octadecanol/F127 mole ratios of (e) 2:1, (f) 10:1, and (g) 15:1, respectively. (h) The evolution of length and aspect ratio along with the octadecanol/F127 mole ratio. SEM images of polymer nanocrescents prepared with different octadecanol/resorcinol mole ratios of (i) 0.02, (j) 0.01, and (k) 0.004, respectively. (l) The evolution of length along with the octadecanol/resorcinol mole ratio and the fitting graph between aspect ratio and octadecanol/resorcinol mole ratio. Scale bars: 200 nm.

octadecanol molecules are rapidly frozen under a significant temperature difference when cooled down at low temperature, leading to mini-nanocrescents with small aspect ratio. To verify the availability of carbon nanocrescents with different aspect ratios, the polymer nanocrescents prepared at different annealing temperatures are pyrolysis at 600 °C to give their carbonaceous analogues. As shown in Fig. S1 in the ESM, carbon nanocrescents retained the morphology features of their polymer precursors. Their length and thickness shrunk by 20%–30%, respectively, while the aspect ratio remained constant roughly.

Next, we studied whether the octadecanol/F127 mole ratio has an impact on the asymmetric assembly process. The SEM images of polymer nanoparticles with mole ratios of octadecanol/F127 = 2:1, 5:1, 10:1, 15:1, and 20:1 have been presented in Figs. 3(e), 1(c), 3(f), and 3(g), and Fig. S2 in the ESM, respectively. When the mole ratio increased from 2:1 to 10:1, i.e., the fraction of hydrophobic octadecanol gradually increased, the length steadily increased from 85 to 147 nm. With a further increase to 15:1 and 20:1, smaller polymer nanocrescents with gradually decreased length together with nanorings as byproducts were observed due to the increasing concentration of primary micelles. Whereas there has been no great change in aspect ratio (Fig. 3(h)), implying a parallel crystallization and assembly behavior at a consistent annealing temperature of 28 °C.

Since the polymerization process provides an alternative method for the morphology regulation of nanoparticles, we further studied the morphology transformation of the polymer nanocrescents prepared with different mole ratios of octadecanol/resorcinol. As shown in Figs. 1(c), 3(i), and 3(j), when the ratio decreased from 0.04 to 0.02 and 0.01, the nanocrescents transformed into soybean-like shape with increased lengths. When the ratio further decreased to 0.004, quasi-spherical nanoparticles with aspect ratio of ~ 1.1 were prepared (Fig. 3(k)). Thus, we hypothesized that the polymer precursors may preferentially grow around the smooth domain to offset the morphology anisotropy. A good linear relationship between the aspect ratio and log(octadecanol/resorcinol mole ratio) was obtained (Fig. 3(l)), of which the linear equation is $y = 1.36x + 1.99$. It shows that we can readily switch the degree of anisotropy of polymer nanocrescents by simply regulating the octadecanol/resorcinol mole ratio in the process of polymerization. To verify the texture structure of the carbon nanocrescents, the $CO_2$ adsorption isotherm and XRD pattern were measured. From the results displayed in Figs. S3(a) and S3(b) in the ESM, the carbon nanocrescents show high surface area (714 $m^2/g$), dominant micropores (0.23 $m^3/g$), narrow pore size distribution (0.5–0.6 nm), and amorphous carbon skeleton.

### 3.3 Insight into the asymmetric assembly mechanism

Figure 4(a) shows the differential scanning calorimetry (DSC) melting curves of neat octadecanol and octadecanol/F127 crescent micelles. There existed one exothermic peak for neat octadecanol at 60.6 °C, and as for the crescent micelles, the exothermic peak appeared at a lower temperature of 55.9 °C, revealing that the F127 coronal would suppress the crystallization of octadecanol and lead to a lower $T_m$ of octadecanol core. Meanwhile, the adverse effect of octadecanol upon F127 led to negligible $T_m$ of crystalline poly(ethylene oxide) (PEO) block [33]. This result firmly demonstrated the interaction between F127 and octadecanol.

Fourier transform infrared (FT-IR) spectra of F127, octadecanol, and the crescent micelles were measured to understand the molecular interaction between F127 and octadecanol (Fig. 4(b)). The peaks at 3236 and 3330 $cm^{-1}$ in neat octadecanol can be ascribed to –OH stretching in γ-phase of octadecanol. In contrast, no evident peak of –OH groups could be found in F127 due to the tiny proportion of –OH groups. Compared with neat octadecanol, the –OH peak at ~ 3230 $cm^{-1}$ in

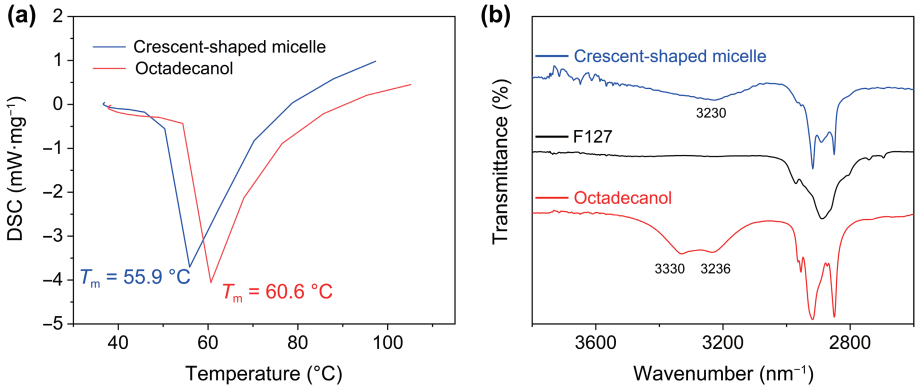

**Figure 4** (a) DSC melting curves of crescent micelles and net octadecanol. (b) FT-IR spectra of neat octadecanol, F127, and crescent micelles.

crescent micelles changes to rounded and broad peak with slight red shift, which can be attributed to the formation of H-bond between octadecanol and F127. According to Ref. [34], primary alcohols have a strong capacity for the formation of hydrogen bonds and interaction with adjacent molecules. Therefore, it is convincing that the –OH groups of octadecanol core may interact with –O– groups of F127 through hydrogen bonds in the crescent micelles.

To gain insight into the mechanism of the formation of crescent-shaped micelles, we studied the morphology transformation during the assembly of F127 and octadecanol through MD simulations in a 100 nm × 100 nm × 100 nm box using a Brownian dynamic algorithm. Two systems with annealing temperatures of 8 and 48 °C are chosen as typical ones, and the detailed model and simulation method are shown in Section S1 and Figs. S4–S6 in the ESM.

In the beginning, the F127 spherical micelles consisting of 800 molecules are pre-assembled and undergo structural relaxation for 50 ns at 80 °C. After that, 4000 octadecanol molecules are added into the hydrophobic core of F127 micelles and followed by structural relaxation at 8 or 48 °C for another 50 ns. Then, elliptical micelles are formed following the first step of the assembly process. We find that the octadecanol aggregators, existing in the form of laminar crystals, asymmetrically distribute within the hydrophobic core after structural relaxation at annealing temperatures. Meanwhile, the hydrophilic blocks at the end of the elliptical micelles cannot enclose well the hydrophobic core, which shows that micelles tend to fuse at the end of micelles (Fig. 5(a)). In addition, we find that the bending angles of most micelles are obtuse angles, and the bending angles of micelles after fusion strongly depend on the fusion angle (Fig. S5 in the ESM). Therefore, in the second step of the assembly, we make two elliptical micelles to fuse along the long axis of them at an obtuse angle (~ 150°) (see Fig. S6 in the ESM for the simulation process). Because of the large molecular structure of F127 and the rigid skeleton of octadecanol crystals within the hydrophobic core of micelles, the partially fused micelle is kinetically locked, giving rise to the formation of anisotropic crescent structures, as shown in Fig. 5(c). It is needed to note that the enclosing of the hydrophilic blocks is influenced by the ratio of octadecanol molecules. According to Figs. S7(a) and S7(b) in the ESM, when the number of octadecanol molecules is excessive (e.g., 15:1), many areas at the end of micelles are needled by the octadecanol crystals, causing more exposure of the hydrophobic section, which then promotes the fusion rate of micelles. While too little amount of octadecanol does not affect how the hydrophilic layer encloses the hydrophobic layer (e.g., 2:1).

Furthermore, the influence of annealing temperature on

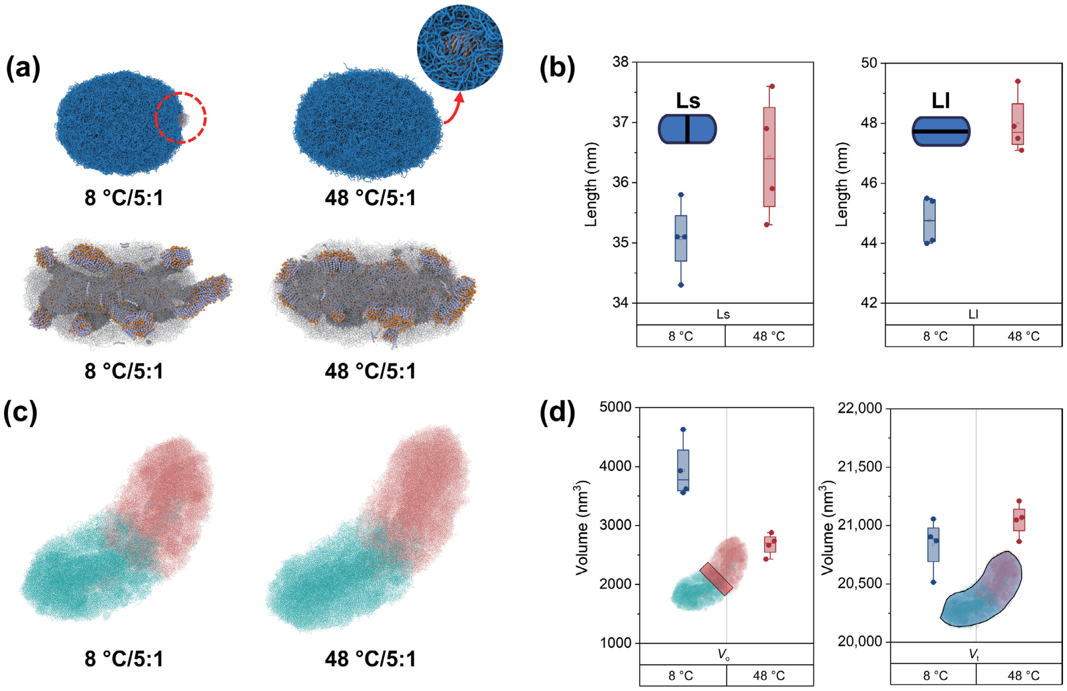

**Figure 5** (a) The morphology of the elliptical micelles following the first step of the assembly process at different temperatures, and the structural details of hydrophobic cores for the corresponding micelles. (b) The Ls and Ll of the elliptical micelles. (c) The whole structure of the crescent micelles after the second step assembly, in which the different elliptical micelles from the first step are described by different colors. (d) The $V_o$ and $V_t$ of the crescent micelles.

morphology was studied. In the case of the elliptical micelles, which are obtained after the first step of the assembly process, the lengths of the short axis (Ls) and long axis (Ll) at 8 °C are shorter than the length at 48 °C, indicating that the low temperature makes micelles shrink (Fig. 5(b)). In addition, the shorter Ll and Ls cause a larger overlapping ratio and smaller total volume under the same fusion depth. Therefore, the overlap volume ($V_o$) decreases and the total volume ($V_t$) of micelles increases with increasing temperature, leading the proportion of $V_o$ to decrease with increasing temperature (Fig. 5(d)). Furthermore, the smaller proportion of $V_o$ promotes the degree of separation for the two elliptical micelles and makes the assembled crescent structure spindlier and the bending angle (An) more obvious (Figs. 6(a) and 6(b)), consistent with the experiments. Regarding the octadecanol molecules, the crystallization process would cause the volume of these molecules to decrease. However, the volume at 48 °C is larger than the volume at 8 °C when the systems are balanced (Fig. 6(c)). Figure 7(a) shows the crystallization process of the octadecanol molecules in detail and the transformation of the packing way along with the relaxation time. Figures 7(b) and 7(c) show that the proportion of the close-packed structures is significantly decreased at 48 °C, leading to the larger volume, and finally inducing the lengthening of the micelles. At 8 °C, however, more close-packed structures make the octadecanol aggregators more rigid, and the micelles shrink with decreasing the temperature at the same time. As a consequence, the octadecanol aggregators are more likely to needle the hydrophilic layer at 8 °C, as shown in Fig. 5(a).

Based on the experiment and simulation study, the morphology transformation mechanism during the assembly of F127 and octadecanol is proposed as follows. Firstly, the crystallization and asymmetric distribution of octadecanol molecules can make the hydrophobic core exposed at the end along the long axis of the elliptical micelles, consequently facilitating the subsequent directional fusion of micelles. Secondly, the large molecular structure of F127 and the octadecanol crystals within the hydrophobic core of micelles can prevent the micelles from diffusing further after the fusion of the elliptical micelles, resulting in the formation of the crescent micelles. Then, lower temperature favors the close-packed structures of octadecanol molecules and smaller volumes of micelles, leading the octadecanol aggregators not to cling to the hydrophobic core and to needle the hydrophilic layer. On the contrary, higher temperature causes smaller $V_o$ and larger $V_t$ under the same fusion depth, making the bending angle more obvious and thus curving the morphology to a great extent.

## 4 Conclusions

In summary, we have reported a facile crystallization-assisted asymmetric assembly synthesis of polymer and carbon nanocrescents based on the asymmetric assembly of amphiphilic F127 and crystalline octadecanol. Theoretical simulations provided fundamental insights into the underlying mechanism of the assembly of crescent micelles and the morphology transformation process as a function of annealing temperature and octadencanol/F127 mole ratio. It is the crystallization of octadecanol molecules that breaks the symmetry of spherical F127/octadecanol micelles and induces the transformation from spherical into elliptical, and finally crescent-shaped. More importantly, the morphology of the nanocrescents is regulable by changing the reaction conditions. We expect these anisotropic nanostructures would serve as a model system and afford a specialized horizon for fundamental study in catalysis, biomedicine, and sensing.

## Acknowledgements

This work was supported by the National Natural Science Foundation of China (Nos. 21875028 and 22288101), Liaoning Revitalization Talents Program (No. XLYC1902045), and the Science and Technology Innovation Fund of Dalian (No. 2020JJ26GX030).

**Electronic Supplementary Material:** Supplementary material (model and simulation method, characterizations, Figs. S1–S7, and references) is available in the online version of this article at https://doi.org/10.1007/s12274-023-5932-3.

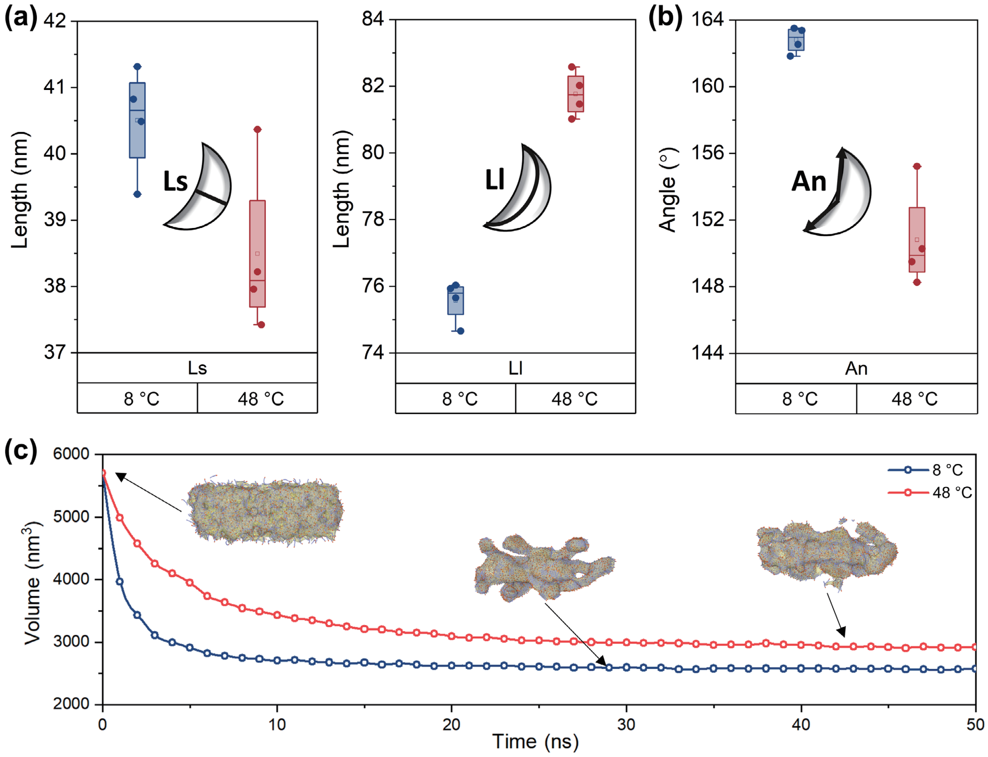

**Figure 6** (a) The Ls and Ll, (b) An, and (c) the volume of the aggregator of octadecanol molecules at 8 and 48 °C.

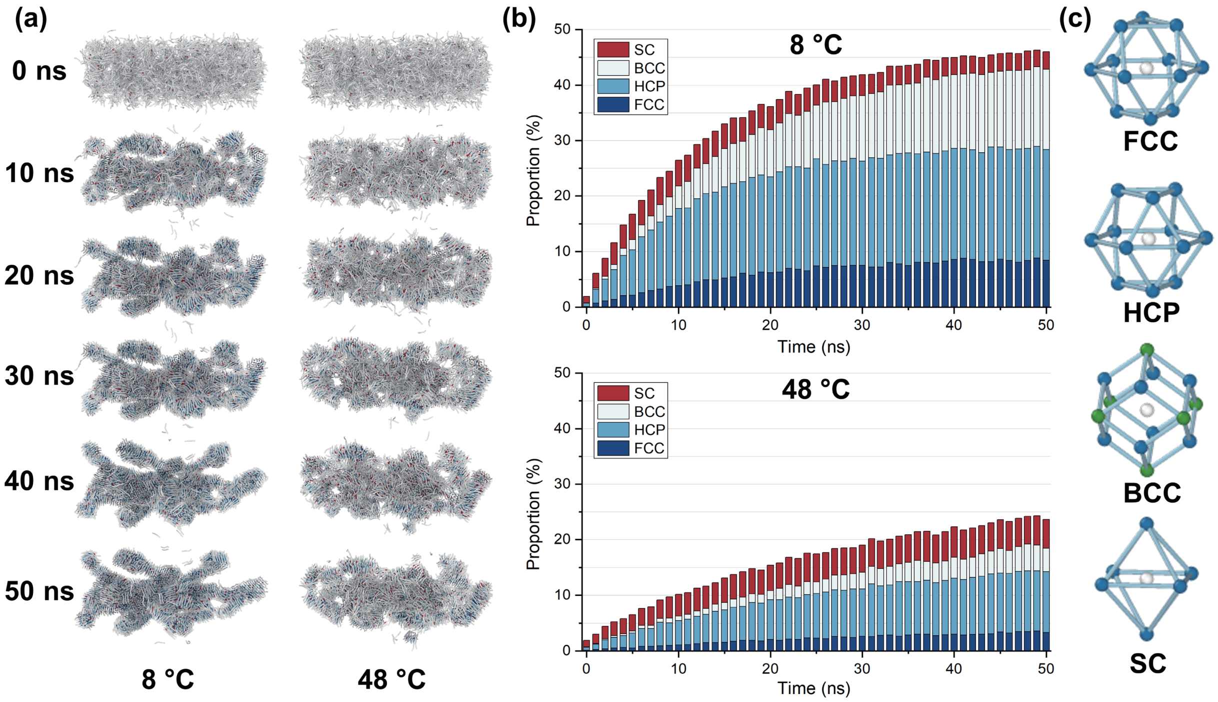

**Figure 7** (a) The crystallization process of octadecanol molecules at 8 °C (left) and 48 °C (right). (b) The evolution of proportion of the face-centered cubic structure (FCC), the close-packed hexagonal structure (HCP), the body-centered cubic structure (BCC), and the simple cube structure (SC) in the aggregator of octadecanol molecules following the time at 8 °C (above) and 48 °C (below). (c) The cell of four packing structures.

## References

[1] Wang, T.; Okejiri, F.; Qiao, Z. A.; Dai, S. Tailoring polymer colloids derived porous carbon spheres based on specific chemical reactions. *Adv. Mater.* **2020**, *32*, 2002475.

[2] Zou, L. L.; Hou, C. C.; Wang, Q. J.; Wei, Y. S.; Liu, Z.; Qin, J. S.; Pang, H.; Xu, Q. A honeycomb-like bulk superstructure of carbon nanosheets for electrocatalysis and energy storage. *Angew. Chem., Int. Ed.* **2020**, *59*, 19627–19632.

[3] Xing, Y.; Du, X.; Xu, T. L.; Zhang, X. J. Janus dendritic silica/carbon@Pt nanomotors with multiengines for $H_2O_2$, near-infrared light and lipase powered propulsion. *Soft Matter* **2020**, *16*, 9553–9558.

[4] Islam, M.; Lantada, A. D.; Mager, D.; Korvink, J. G. Carbon-based materials for articular tissue engineering: From innovative scaffolding materials toward engineered living carbon. *Adv. Healthc. Mater.* **2022**, *11*, 2101834.

[5] Gawande, M. B.; Fornasiero, P.; Zbořil, R. Carbon-based single-atom catalysts for advanced applications. *ACS Catal.* **2020**, *10*, 2231–2259.

[6] Guan, B. Y.; Zhang, S. L.; Lou, X. W. Realization of walnut-shaped particles with macro-/mesoporous open channels through pore architecture manipulation and their use in electrocatalytic oxygen reduction. *Angew. Chem., Int. Ed.* **2018**, *57*, 6176–6180.

[7] Yuan, Y. F.; Wang, Y. S.; Zhang, X. L.; Li, W. C.; Hao, G. P.; Han, L.; Lu, A. H. Wiggling mesopores kinetically amplify the adsorptive separation of propylene/propane. *Angew. Chem., Int. Ed.* **2021**, *60*, 19063–19067.

[8] Liu, D.; Gu, W. Y.; Zhou, L.; Wang, L. Z.; Zhang, J. L.; Liu, Y. D.; Lei, J. Y. Recent advances in MOF-derived carbon-based nanomaterials for environmental applications in adsorption and catalytic degradation. *Chem. Eng. J.* **2022**, *427*, 131503.

[9] Chen, C. H.; Xie, L.; Wang, Y. Recent advances in the synthesis and applications of anisotropic carbon and silica-based nanoparticles. *Nano Res.* **2019**, *12*, 1267–1278.

[10] Wang, K.; Li, C.; Li, Z.; Li, H. Z.; Li, A.; Li, K. X.; Lai, X. T.; Liao, Q.; Xie, F.; Li, M. Z. et al. A facile fabrication strategy for anisotropic photonic crystals using deformable spherical nanoparticles. *Nanoscale* **2019**, *11*, 14147–14154.

[11] Zhang, C. C.; Wu, Z. Y.; Chen, Z. J.; Pan, L. B.; Li, J.; Xiao, M. Q.; Wang, L. W.; Li, H.; Huang, Z.; Xu, A. B. et al. Photonic nanostructures of nanodiscs with multiple magneto-optical properties. *J. Mater. Chem. C* **2020**, *8*, 16067–16072.

[12] Zhang, X. E.; Chen, X.; Ren, H. J.; Diao, G. W.; Chen, M.; Chen, S. W. Bowl-like C@$MoS_2$ nanocomposites as anode materials for lithium-ion batteries: Enhanced stress buffering and charge/mass transfer. *ACS Sustainable Chem. Eng.* **2020**, *8*, 10065–10072.

[13] Wu, Z.; Yuan, L.; Han, Q. R.; Lan, Y.; Zhou, Y. J.; Jiang, X. H.; Ouyang, X. P.; Zhu, J. W.; Wang, X.; Fu, Y. S. Phosphorous/oxygen co-doped mesoporous carbon bowls as sulfur host for high performance lithium-sulfur batteries. *J. Power Sources* **2020**, *450*, 227658.

[14] Xie, L.; Yan, M.; Liu, T. Y.; Gong, K.; Luo, X.; Qiu, B. L.; Zeng, J.; Liang, Q. R.; Zhou, S.; He, Y. J. et al. Kinetics-controlled super-assembly of asymmetric porous and hollow carbon nanoparticles as light-sensitive smart nanovehicles. *J. Am. Chem. Soc.* **2022**, *144*, 1634–1646.

[15] Zhao, T. C.; Zhang, X. M.; Lin, R. F.; Chen, L.; Sun, C. X.; Chen, Q. W.; Hung, C. T.; Zhou, Q. Y.; Lan, K.; Wang, W. X. et al. Surface-confined winding assembly of mesoporous nanorods. *J. Am. Chem. Soc.* **2020**, *142*, 20359–20367.

[16] Peng, L.; Peng, H. R.; Xu, L.; Wang, B. X.; Lan, K.; Zhao, T. C.; Che, R. C.; Li, W.; Zhao, D. Y. Anisotropic self-assembly of asymmetric mesoporous hemispheres with tunable pore structures at liquid-liquid interfaces. *J. Am. Chem. Soc.* **2022**, *144*, 15754–15763.

[17] Xuan, M. J.; Mestre, R.; Gao, C. Y.; Zhou, C.; He, Q.; Sánchez, S. Noncontinuous super-diffusive dynamics of a light-activated nanobottle motor. *Angew. Chem., Int. Ed.* **2018**, *57*, 6838–6842.

[18] Wang, W. X.; Wang, P. Y.; Chen, L.; Zhao, M. Y.; Hung, C. T.; Yu, C. Z.; Al-Khalaf, A. A.; Hozzein, W. N.; Zhang, F.; Li, X. M. et al. Engine-trailer-structured nanotrucks for efficient Nano-bio interactions and bioimaging-guided drug delivery. *Chem* **2020**, *6*, 1097–1112.

[19] Cai, J. D.; Manners, I.; Qiu, H. B. "Self-adaptive" coassembly of colloidal "saturn-like" host–guest complexes enabled by toroidal micellar rubber bands. J. Am. *Chem. Soc.* **2022**, *144*, 5734–5738.

[20] Avendaño, C.; Jackson, G.; Müller, E. A.; Escobedo, F. A. Assembly of porous smectic structures formed from interlocking high-symmetry planar nanorings. *Proc. Natl. Acad. Sci. USA* **2016**, *113*, 9699–9703.

[21] Luo, Y.; Lei, D. Y.; Maier, S. A.; Pendry, J. B. Broadband light harvesting nanostructures robust to edge bluntness. *Phys. Rev. Lett.* **2012**, *108*, 023901.

[22] Rochholz, H.; Bocchio, N.; Kreiter, M. Tuning resonances on crescent-shaped noble-metal nanoparticles. *New J. Phys.* **2007**, *9*, 53.

[23] Giordano, M. C.; Foti, A.; Messina, E.; Gucciardi, P. G.; Comoretto, D.; de Mongeot, F. B. SERS amplification from self-organized arrays of plasmonic nanocrescents. *ACS Appl. Mater. Interfaces* **2016**, *8*, 6629–6638.

[24] Wu, L. Y.; Ross, B. M.; Lee, L. P. Optical properties of the crescent-shaped nanohole antenna. *Nano Lett.* **2009**, *9*, 1956–1961.

[25] Dostert, K. H.; Álvarez, M.; Koynov, K.; Del Campo, A.; Butt, H. J.; Kreiter, M. Near field guided chemical nanopatterning. *Langmuir* **2012**, *28*, 3699–3703.

[26] Jang, H. J.; Jung, I.; Zhang, L. Q.; Yoo, S.; Lee, S.; Cho, S.; Shuford, K. L.; Park, S. Asymmetric Ag nanocrescents with Pt rims: Wet-chemical synthesis and optical characterization. *Chem. Mater.* **2017**, *29*, 5364–5370.

[27] Wang, Y.; Li, Z.; Shmidov, Y.; Carrazzone, R. J.; Bitton, R.; Matson, J. B. Crescent-shaped supramolecular tetrapeptide nanostructures. *J. Am. Chem. Soc.* **2020**, *142*, 20058–20065.

[28] Hou, L.; Li, W. C.; Liu, C. Y.; Zhang, Y.; Qiao, W. H.; Wang, J.; Wang, D. Q.; Jin, C. H.; Lu, A. H. Selective synthesis of carbon nanorings via asymmetric intramicellar phase-transition-induced tip-to-tip assembly. *ACS Cent. Sci.* **2021**, *7*, 1493–1499.

[29] Plimpton, S.; Crozier, P.; Thompson, A. LAMMPS-large-scale atomic/molecular massively parallel simulator. *Sandia Natl. Lab.* **2007**, *18*, 43. https://www.lammps.org/#gsc.tab=0

[30] Arnarez, C.; Uusitalo, J. J.; Masman, M. F.; Ingólfsson, H. I.; De Jong, D. H.; Melo, M. N.; Periole, X.; De Vries, A. H.; Marrink, S. J. Dry martini, a coarse-grained force field for lipid membrane simulations with implicit solvent. *J. Chem. Theory Comput.* **2015**, *11*, 260–275.

[31] Stukowski, A. Visualization and analysis of atomistic simulation data with OVITO—The open visualization tool. *Modelling Simul. Mater. Sci. Eng.* **2010**, *18*, 015012.

[32] Tang, J.; Yang, M.; Yu, F.; Chen, X. Y.; Tan, L.; Wang, G. 1-Octadecanol@hierarchical porous polymer composite as a novel shape-stability phase change material for latent heat thermal energy storage. *Appl. Energy* **2017**, *187*, 514–522.

[33] Yang, J. X.; Fan, B.; Li, J. H.; Xu, J. T.; Du, B. Y.; Fan, Z. Q. Hydrogen-bonding-mediated fragmentation and reversible self-assembly of crystalline micelles of block copolymer. *Macromolecules* **2016**, *49*, 367–372.

[34] Acquah, C.; Cagnetta, M.; Achenie, L. E. K.; Suib, S. L.; Karunanithi, A. T. Effect of solvent topography and steric hindrance on crystal morphology. *Ind. Eng. Chem. Res.* **2015**, *54*, 12108–12113.